



## Full Length Article

## Polarized-SERS of non-isotropic molecules on thermally-induced corrugated plasmonic surface supporting a NIR-SPP mode

Ephraim Mathew<sup>a</sup>, Jacek Jenczyk<sup>a</sup>, Zygmunt Miłosz<sup>a</sup>, Joel Henzie<sup>b</sup>, Igor Iatsunskyi<sup>a</sup>, Patryk Florczak<sup>a</sup>, Weronika Andrzejewska<sup>a</sup>, Mikołaj Lewandowski<sup>a</sup>, Maciej Wiesner<sup>c,\*</sup><sup>a</sup> NanoBioMedical Centre, Adam Mickiewicz University, Wszechnicy Piastowskiej 3, 61-614 Poznań, Poland<sup>b</sup> Research Centre for Materials Nano Architectonics, National Institute for Materials Science (NIMS), 1-1 Namiki, Tsukuba, Ibaraki 305-0044, Japan<sup>c</sup> Faculty of Physics, Adam Mickiewicz University, Uniwersytetu Poznańskiego 2, 61-614 Poznań, Poland

## ARTICLE INFO

## Keywords:

NIR-surface plasmon polaritons  
Long-range periodic nanostructure  
Percolated ultrathin film plasmonics  
Non-isotropic molecules on corrugated plasmonic surface  
Polarized surface enhanced Raman spectroscopy  
Dichroic SERS effect  
Large area SERS sensing

## ABSTRACT

Thermally-induced surface reconstruction of  $\alpha$ -Al<sub>2</sub>O<sub>3</sub> was used to fabricate corrugated templates of different periods to support percolated ultrathin metal film. Reflectance analysis and simulations revealed the coupling of a hybrid NIR-SPP mode along its corrugation vector ( $k_{\text{corrugation}}$ ). The fabricated samples enhanced Raman signals of phenyl thiolates (PT) with reduced photo-induced disadvantages at  $\lambda_{\text{exc}} = 785$  nm. Polarized SERS were performed to study adsorbed molecule – polariton interaction on these corrugated thin film surface. A twofold SERS anisotropy with a  $\cos^2(\sigma)$  dependency ( $\sigma$  = azimuthal angle) was observed. SERS dichroism of PT Raman modes of different polarizability tensors were analysed. A more pronounced dependence on corrugation period was observed for totally symmetric  $a_1$  modes than the non-totally symmetric  $b_1$  and  $b_2$  modes. Apart from the relative SERS intensity, their SERS dichroism was determined mostly by the excitation of SPP along the  $k_{\text{corrugation}}$  rather than the orientation of PT on sample surface. Edge-on orientation of adsorbed PT was predicted due to the absence of  $a_2$  modes with both tensor components parallel to the surface. Shorter corrugation periods fabricated were reproducible and ample for uniform, large-area sensing due to effective SPP coupling at  $\sigma = 0^\circ$  resulting in a spatially extended SERS excitation volume.

## 1. Introduction

Surface-enhanced Raman spectroscopy (SERS) is a rapidly advancing superlative “surface sensing” technique in recent decades [1,2]. A key factor giving rise to SERS effect is the enhanced electromagnetic (EM) near field generated by surface plasmons. Excitation of Raman active modes and its re-radiation as scattering signal is amplified for molecules present within this enhanced field. Maximum near-field enhancement and effective SERS response are achieved when the excitation wavelength  $\lambda_{\text{exc}}$  and the corresponding analytes Stokes-shifted wavelength ( $\lambda_{\text{stokes}}$ ) is within the bandwidth of the excited plasmon mode [3]. However, SERS substrates exhibiting plasmon resonance in the UV–visible range induces photochemical reactions [4,5] such as photobleaching [6,7], photo-degradation [8,9], desorption of self-assembled monolayers [10] and interference effects due to fluorescence resulting from both analyte and metal surface [11–13]. Utilizing  $\lambda_{\text{exc}}$  in the near-infrared (NIR) wavelength reduces the energy transferred to the system, minimizing photo-induced effects on analytes, and sample degradation

[14–16]. For this reason, the fabrication and design of substrates exhibiting plasmon resonance in the NIR range is desirable. Substrates decorated with metal nanoparticles (NPs) exhibit localized surface plasmon resonance (LSPR) and are the most commonly used NIR-SERS substrates due to their high order of near field enhancement ( $10^{10}$ ) [17,18] and scattering coefficient [19,20]. These tightly focused localized fields on NPs edges known as hotspot facilitates the higher orders of SERS enhancement. However, laterally continuous periodic metal films can support “propagating” surface plasmon polariton (SPPs) modes, which generates a distributed EM near field, spatially extending the SERS excitation volume [21–23]. This relieves the analytes necessity of a closer location to the hotspot as NP arrays sporadically suffers from overlapping of clusters and aggregation during fabrication [24,25]. Further, these SPP supporting structures have a diverse range of applications such as on chip communications [26], waveguides [27], THz devices [28] and in increasing the spatial resolution of scanning near field microscopy (SNOM) [29]. In this work, we demonstrate a well-established temperature-induced surface reconstruction of ( $\alpha$ -Al<sub>2</sub>O<sub>3</sub>) [30]

\* Corresponding author.

E-mail address: [mwiesner@amu.edu.pl](mailto:mwiesner@amu.edu.pl) (M. Wiesner).<https://doi.org/10.1016/j.apsusc.2024.159821>

Received 11 December 2023; Received in revised form 7 February 2024; Accepted 1 March 2024

Available online 2 March 2024

0169-4332/© 2024 The Authors. Published by Elsevier B.V. This is an open access article under the CC BY license (<http://creativecommons.org/licenses/by/4.0/>).

technique, that can be used to fabricate large-area (2x2cm) templates of different corrugation periods for ultra-thin Au film deposition towards plasmonic applications. The fabrication mechanism of the templates is already well described in Ref.[31]. The Au metal deposited periodic nanostructures diffract light with an increased wavevector, mediating plasmon-photon momentum matching conditions [32]. This excludes the requirement of complex optical setup such as end coupling, tapered coupling and prism to excite SPPs [33]. However, for non-isotropic molecules such as phenyl-thiolates (PT) adsorbed on surfaces apart from the plasmon resonance wavelength ( $\lambda_{SPP}$ ) the polarization and strength of the electric field components on surface influences the relative Raman peak intensities based on the molecule's Raman polarizability tensor ( $\alpha$ ) [34]. "Surface selection rules" based on varying band intensities of SERS spectrum for molecules adsorbed on surface of metal was proposed in Refs. [35,36]. Studies such as depolarization measurements of non-isotropic molecules [37] and SERS of thiolates in different refractive index medium [38] were performed to study the ratio of relative Raman intensities and predict the orientation of adsorbed molecules on surface. These SERS studies on adsorbed organothiol layers on the metal surfaces have a strong applicative relevance towards chemical sensing, molecular electronics, wetting and lubrication applications as in Ref [39]. Here, we study the SERS effect of phenyl-thiolates adsorbed on the fabricated corrugated plasmonic surface, which can support propagating SPP in the NIR range. These substrates generate large electric field components parallel and perpendicular to the surface during SPP excitation based on their  $k_{corrugation}$ . Ref.[40] proved the selective enhancement of Raman dipole moments parallel to nano wire-wire cavity in nanowire gratings through polarized SERS measurements. Similarly on these uniaxial corrugated thin films field polarizations play an important role due to excitation of SPP only in polarization along the  $k_{corrugation}$ . Polarized SERS measurements were performed to investigate the corrugation-induced plasmonic anisotropy and adsorbed molecule – polariton interaction. Molecular vibration – polariton coupling on gratings is a topic with growing interest due to its vast potential in multiple fields as in Refs [41–43]. Particularly in developing emissive devices such as OLED (Organic LED) [44] and dye lasers [45], where the molecular emitters on the surface of periodic metal nanostructures couple to the near field SPP mode and re-radiate their energy as Bragg scattered light. The objective of this article is to investigate the PT molecule vibrations - polariton interaction through polarized SERS measurement. As the excited SPPs near field in NIR ranges have large molecule dipole oscillator strength [41], and exhibit reduced photo-induced disadvantages, such as charge transfer and interference background signal in spectra. A twofold SERS anisotropy of PT molecules was observed in polarized SERS. SERS dichroism of PT Raman vibration modes of different polarizability tensors were analyzed and reported. Moreover, SERS substrates based on NP arrays and nanowire gratings supporting NIR-LSPR modes and their SERS phenomena were demonstrated and described in recent studies [46–49]. However, NIR-SPP mode supporting laterally continuous corrugated metal thin films, their related SERS enhancement and topography induced SERS anisotropies of adsorbed molecules are not demonstrated and extensively studied based on our findings in literature. Our study show the dependence of SPP modes surface field orientations on corrugated surface with different  $k_{corrugation}$  in the enhancement of both the diagonal and non-diagonal components of  $\alpha$ . SERS substrate reproducibility and large-area sensing uniformity were tested. Finally, the positives and drawbacks of the fabricated samples in SERS application are discussed.

## 2. Experimental details

### 2.1. Sample fabrication method

Sapphire ( $\alpha$ -Al<sub>2</sub>O<sub>3</sub>) single crystals with a  $< 0.1^\circ$  miscut along the

**Table 1**

Structural parameters of the fabricated samples.

| Sample name                | (Sa1)<br>Au<br>thickness<br>=10 nm | (Sa2)<br>Au thickness<br>=10 nm | (Sa3)<br>Au thickness<br>=10 nm | (Sa4)<br>Au thickness<br>=10 nm |
|----------------------------|------------------------------------|---------------------------------|---------------------------------|---------------------------------|
| Substrate                  | flat                               | 170 $\pm$ 25<br>nm              | 290 $\pm$ 25<br>nm              | 450 $\pm$ 30<br>nm              |
| Corrugation<br>period [nm] | flat                               | 19 $\pm$ 5 nm                   | 30 $\pm$ 5 nm                   | 35 $\pm$ 10 nm                  |

M-plane [10 $\bar{1}$ 0] were commercially purchased from CrysTec GmbH. When annealed at high temperatures ( $T > 1400^\circ\text{C}$ ), the unstable crystallographic plane undergoes spontaneous asymmetric faceting, which leads to the formation of periodic, corrugated structures on the surface, which was desirable for the experiment [30]. A carbolite high-temperature chamber furnace was used to treat the substrates at operating temperatures up to  $1700^\circ\text{C}$ . Depending on the annealing time (between 12 and 24 h) and temperature ( $1450$  to  $1550^\circ\text{C}$ ), the period of naturally forming sapphire surface corrugations varied. An electron beam evaporation system (Telemark/PREVA) was used to deposit a 10 nm thick layer of Au from a sapphire crucible at a low deposition rate of  $79 \text{ \AA} / \text{hour}$  onto flat and reconstructed surface templates (Table 1). Before Au deposition, all samples were outgassed at a temperature of  $550^\circ\text{C}$  for 1 h. After the deposition, the samples were annealed again at  $300^\circ\text{C}$  for 20 min. The degassing, deposition and annealing were performed under ultra-high vacuum (UHV) conditions ( $10^{-10}$  mbar) - Figure S1.

### 2.2. Structural and optical characterization

The topography of fabricated plasmonic substrates was determined using the Bruker Dimension Icon atomic force microscope (AFM) working in soft tapping mode.  $10 \times 10 \mu\text{m}^2$  scans were recorded at different places on the sample to analyse the corrugated surface. Reflectance analysis of the samples was performed using the SENTECH GmbH SER800 ellipsometer at an oblique incidence angle  $\theta = 50^\circ$ . Transverse magnetic (TM) and transverse electric (TE) polarization components of the corrugated plasmonic substrates were collected in the spectral range from 400 to 1050 nm with a scanning interval of 1 nm. All the reflectance measurements were normalized to a reference signal collected from a 99.99 % reflecting mirror.

### 2.3. Simulation technique

To model the optical properties of Au, we used the optical constants described by Rosenblatt et al [50] for an 11-nm thick Au film. The optical properties of sapphire were modelled using the properties of Al<sub>2</sub>O<sub>3</sub> described by Palik [51]. The Au/Al<sub>2</sub>O<sub>3</sub> periodic structure (Sa2) see Table 1. with a corrugation period of 170 nm was drawn in an EM solver (Lumerical Solutions), then a conformal 10 nm thick Au film was added on top of the corrugated Al<sub>2</sub>O<sub>3</sub> surface. The simulations were performed utilizing periodic boundary conditions and was excited with a TM polarized plane wave (PW) at  $\theta = 0^\circ$  and  $50^\circ$ . The PW source had a narrow bandwidth (FWHM = 0.5 nm) to increase the precision of the calculation and minimize material dispersion effects. The electric field intensity ( $|E|^2$ ) was collected by taking the square magnitude of the electric field vector in 3D space (i.e.  $|E_x|^2 + |E_y|^2 + |E_z|^2$ ) in the plane of the corrugated Au surface. The spatial distribution of the charge polarization imposed by the plasmon mode is represented by plotting the divergence of the electric field ( $\nabla E$ ) in the plane of the corrugated surface.

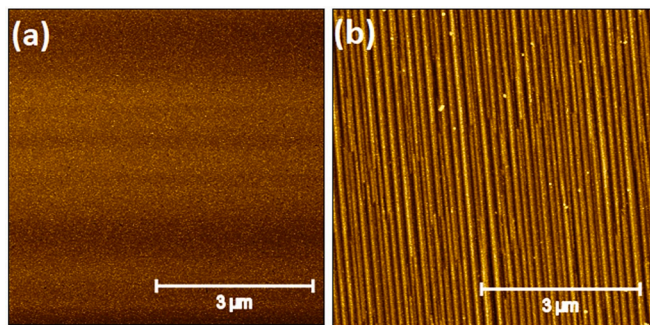


**Fig. 1.** AFM images of (a) flat non-reconstructed plasmonic sample (Sa1) and (b) reconstructed corrugated plasmonic sample (Sa2).

#### 2.4. Organic molecules deposition

The fabricated plasmonic substrates were immersed in a solution of 99.8 % thiophenol (Alfa Aesar) dissolved in 99.8 % ethanol (POCH) (1:50 vol). After 10 min at RT, the samples were removed from the thiophenol solution and consequently immersed in pure ethanol to remove unbonded molecules. The whole process was repeated four times to form a layer of thiophenol molecules bonded to the Au surface [52]. As-prepared samples were investigated using Raman spectroscopy.

#### 2.5. SERS measurements

Micro-Raman spectra were measured using a commercial Renishaw inVia micro-Raman system with a 633 and 785 nm plane-polarized laser. All spectra were measured under a 0.7 N.A microscopic objective within an aperture angle of 50°; 4 accumulations with 1 s exposure time scans were collected. A spectral resolution of about  $1 \text{ cm}^{-1}$  was achieved using a 1200 and 1800 l/mm grating for the respective laser wavelengths. A STANDA 050097 rotational step motor stage was used to perform polarized SERS measurement for an azimuthal angle  $\sigma$  determined between the laser polarization and the corrugation vector with an angle step  $\Delta\sigma = 2.5^\circ$ . SERS mapping measurements were performed by scanning the laser spot at 3 μm steps to check the large-scale uniformity of SERS signal on the samples.

### 3. Results and discussion

The thermodynamically unstable flat ( $\alpha\text{-Al}_2\text{O}_3$  -10 $\bar{1}0$  plane) surface, with a high surface energy density reconstructed into corrugated hill and valley structures to attain an equilibrium with reduced total surface energy planes, during annealing (see sample fabrication section) [53]. Such large area formation of one dimensionally oriented surface modulations are viewed as sophisticated optical devices which are difficult to fabricate in a mechanically hard and robust substrate such as sapphire. Here we utilize the anisotropy of sapphire single crystal with a miscut crystallographic plane to produce thermally induced spontaneous faceting of corrugated surface structures extending all over the (2x2cm)

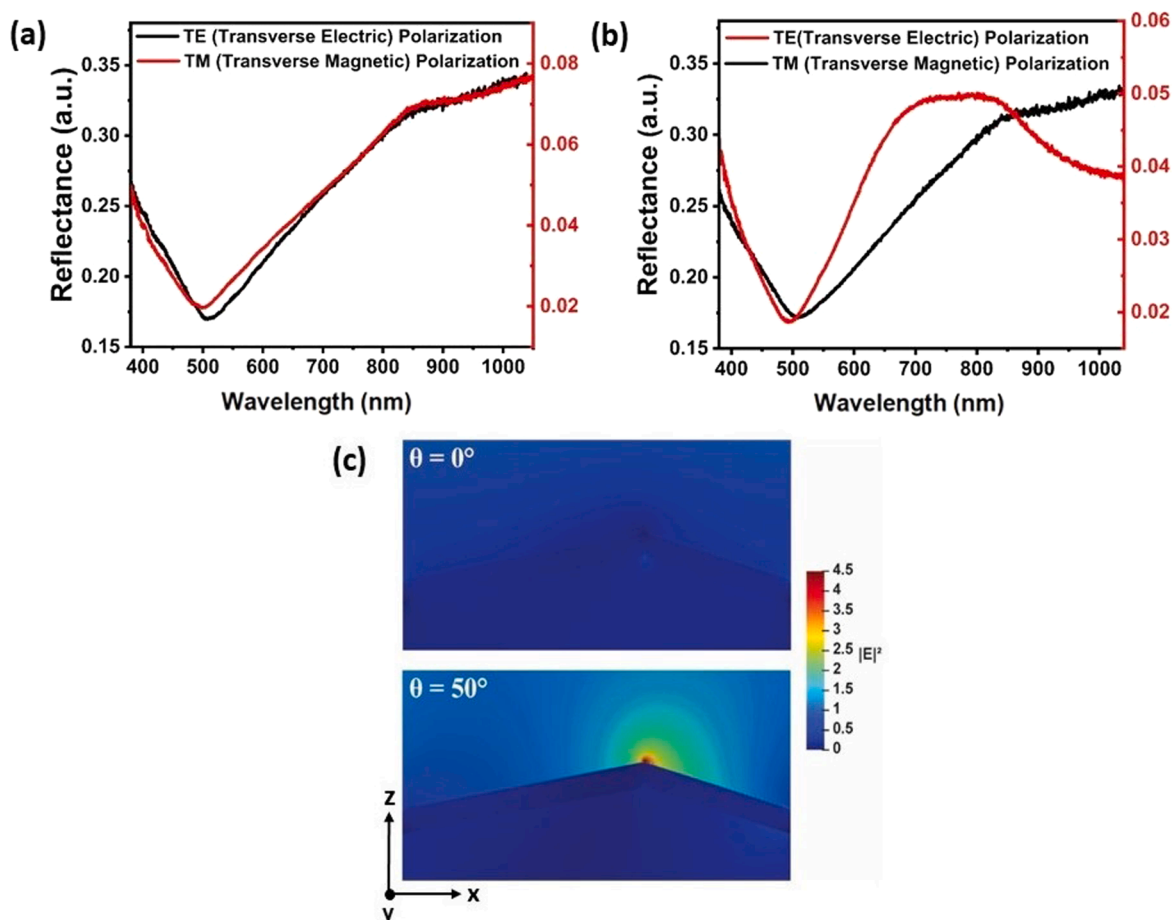


**Fig. 2.** (a) Reflectance measurements of 10 nm Au film on flat template-Sa1 at  $\theta = 50^\circ$  exhibiting percolated thin film characteristics. (b) Reflectance measurements of the percolated 10 nm Au film on the corrugated sample Sa2 at  $\theta = 50^\circ$  showing a broad dip in the IR region for TM polarization related to the coupling of a hybrid SPP mode, (c) simulated electric field intensity ( $|E|^2$ ) distribution of sample Sa2 for TM polarization,  $\lambda_{\text{inc}} = 785 \text{ nm}$  at  $\theta = 0^\circ$  and  $50^\circ$  exhibiting enhanced optical near field on the corrugated surface at  $\theta = 50^\circ$ .

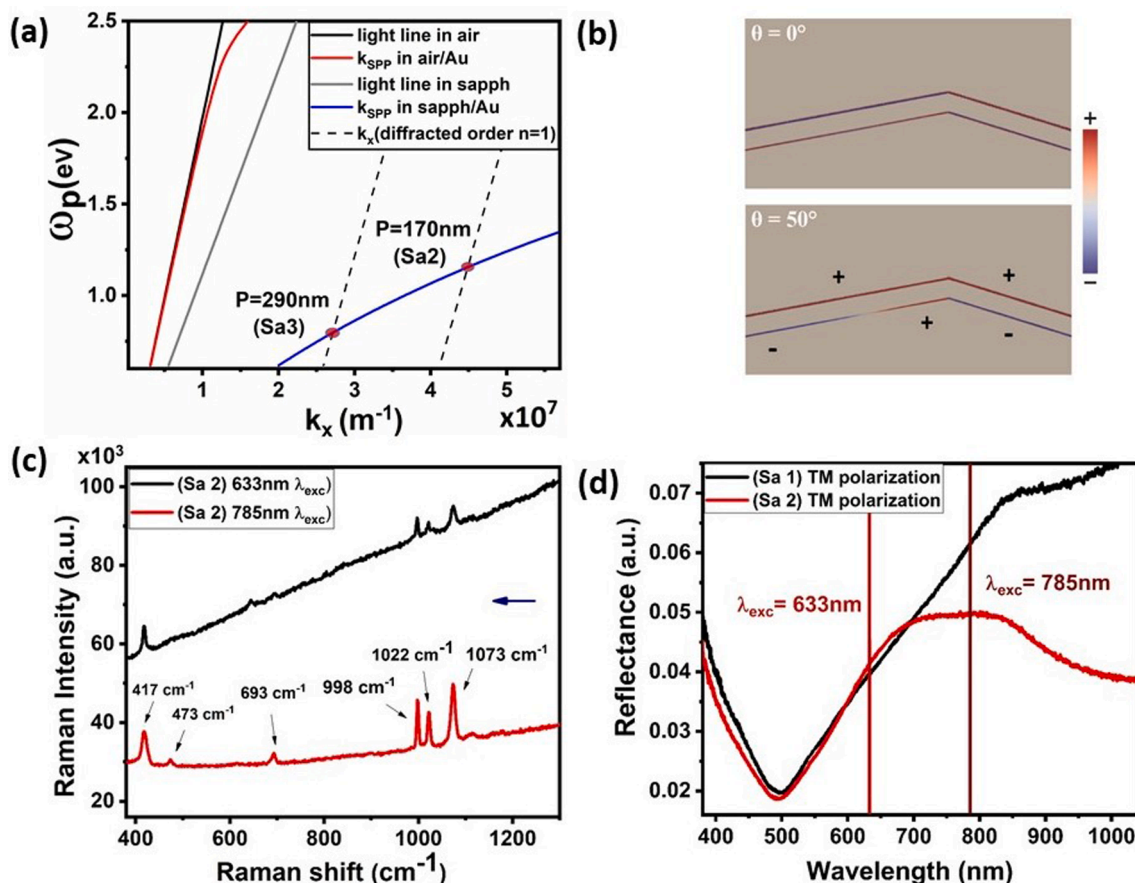


**Fig. 3.** (a) Dispersion curves for Sa2 and Sa3 samples for diffraction order  $n = 1$ . Incident light  $k_{inc}$  (solid black line), resulting diffracted orders  $k_x$  (dashed black line),  $P$  = corrugation periods,  $k_{SPP}$  in air/Au interface = (red line),  $k_{SPP}$  in sapphire/Au interface = (blue line), SPP coupling points (red dots), (b) simulated charge density polarization on the metal dielectric interfaces of Sa2 for TM polarization at  $\lambda_{inc} = 785$  nm at  $\theta = 0^\circ$  and  $50^\circ$  exhibiting the excited hybrid SPP mode excitation at  $\theta = 50^\circ$ , (c) SERS spectra of phenyl thiolate on Sa2 with  $\lambda_{exc} = 633$  nm (black line) and  $\lambda_{exc} = 785$  nm (red line), the blue arrow indicates the downshifting of peaks associated with phenyl ring vibrations upon chemisorption on Au (Raman spectra are presented without fluorescence background subtraction) and (d) Reflectance measurements of sample Sa1 (black spectra) and Sa2 (red spectra) at  $\theta = 50^\circ$ , TM polarization, with the respective Raman laser line positions at  $\lambda_{exc} = 633$  nm and 785 nm.

commercially purchased sapphire wafer. The temporal evolution of its reconstruction phases proceeds as: (a) surface smoothening, (b) nucleation of individual facets, (c) interaction between facets to form facet domains, (d) coalescence of facet domains and (e) facet coarsening as reported in Ref. [31]. Here, these spontaneous processes in the stage of coarsening were optimized to fabricate structures with different periods as shown in Figure S2. Two facets merge into one facet at a point called a facet junction during coarsening. A completely faceted surface can increase its corrugated period/facet wavelength based on the motion and elimination of these junctions. The uniformity of the fabricated structures decreased with increasing value of period  $P$  due to the high degree of node misalignment during facet merging [31]. The most uniform periodicities were observed for a short annealing time at a constant temperature. Fig. 1 shows AFM images of 10 nm of Au deposited onto a flat non-reconstructed template (Fig. 1a) and onto a reconstructed corrugated template (Fig. 1b). In the case of the corrugated template, the Au layer follows the modulation induced by the corrugated facets. Gold was chosen for its chemical stability [54], non-oxidative nature [55] and its ability to support surface plasmons in the NIR range [56]. Metal films with thickness ( $t \sim 8$ –10 nm) near the percolation threshold undergo the transition from a non-conductive (localized electrons) to conductive (high mobility free electrons) with Drude metal characteristics [57,58], which are desirable for the excitation of SPP modes [59,60]. The low-temperature post-deposition annealing step (see sample fabrication section) further improved the film interconnectivity and quenched the

localized plasmon resonance of the percolated 10 nm thick Au film before dewetting process, which occurs at higher annealing temperatures [61,62]. Reflectance analysis of the sample Sa1 (Fig. 2a) confirmed the percolation of Au film with increasing reflectance for the longer wavelengths typical for connected (percolated) metal films [63,57] and a dip near 500 nm wavelength corresponding absorption due to intra-band transitions in Au [64]. The small peak at 831 nm in the spectra results not from a plasmon resonance but from the  $\alpha$ -Al<sub>2</sub>O<sub>3</sub> template; see supporting information - Figure S4. For sample Sa2 (Fig. 2b), the introduction of the periodic modulations resulted in a broad dip at the NIR region for TM polarization component, indicating the coupling of a SPP mode. EM simulations were performed on a Al<sub>2</sub>O<sub>3</sub>/Au corrugated structure modelled using the optical constants for Au described by Rosenblatt et al [50], for a 11-nm thick Au film. Fig. 2c shows the electric field intensity ( $|E|^2$ ) distribution maps using  $\lambda_{inc} = 785$  nm at  $\theta = 0^\circ$  and  $50^\circ$  for TM polarization. The simulated  $|E|^2$  distribution shows the enhanced optical near field along  $E_x$  and  $E_z$  on the surface of the corrugation due to the strong coupling of the SPP mode at  $\theta = 50^\circ$  with a larger wavevector. The SPP coupling takes place at selected momentum-matching conditions between the photons and surface plasmon modes. Corrugated surface structures with  $k_{corrugation}$  dependent on their period  $P$  (see eq. 1) increases the momentum of the diffracted waves  $k_x$  based on the eq.2 [65,66].

$$k_{corrugation} = n \frac{2\pi}{P} \quad (1)$$



**Table 2**

Assignment of thiophenol molecular vibrations and their Raman peak positions with related Stokes wavelengths and symmetry classes of vibration modes [38,77].

| PT Raman vibrations peak positions | Stokes shifted wavelength $\lambda_{\text{stokes}}$ at ( $\lambda_{\text{exc}} = 633$ nm) | Stokes shifted wavelength $\lambda_{\text{stokes}}$ at ( $\lambda_{\text{exc}} = 785$ nm) | PT molecular vibrations assignment                 | Symmetry class ( $C_{2v}$ ) |
|------------------------------------|---|---|--|-----------------------------|
| 473 $\text{cm}^{-1}$               | 652 nm  | 815 nm  | Out-of-plane C-C-C bending                         | $b_1$                       |
| 615 $\text{cm}^{-1}$               | 658 nm  | 824 nm  | In-plane C - C - C ring bending + C - S stretching | $b_2$                       |
| 693 $\text{cm}^{-1}$               | 662 nm  | 830 nm  | In-plane C - C - C ring bending + C - S stretching | $a_1$                       |
| 737 $\text{cm}^{-1}$               | 663 nm  | 833 nm  | Out-of-plane C - H ring bend                       | $b_1$                       |
| 998 $\text{cm}^{-1}$               | 675 nm  | 851 nm  | C - C - C ring bend (ring breathing)               | $a_1$                       |
| 1072 $\text{cm}^{-1}$              | 679 nm  | 857 nm  | In-plane C - C - C bend + C - S stretching         | $a_1$                       |
| 1573 $\text{cm}^{-1}$              | 703 nm  | 895 nm  | Symmetric in-plane C - C ring stretching           | $a_1$                       |

$$k_x = k_{\text{inc}} \sin \theta + n \frac{2\pi}{P} \quad (2)$$

$$k_{\text{SPP}} = \frac{\omega_{\text{SPP}}}{v} \sqrt{\frac{\epsilon_1 \epsilon_2}{\epsilon_1 + \epsilon_2}} \quad (3)$$

where  $k_{\text{inc}}$  = wavevector of the incident light,  $k_{\text{corrugation}}$  = spatial wavevector of corrugation period,  $k_x$  = wavevector of diffracted light order,  $k_{\text{SPP}}$  = SPP wavevector,  $n = 0; \pm 1; \pm 2$ ; diffraction orders,  $\theta$  = incidence angle,  $P$  is the grating period,  $\epsilon_1$  and  $\epsilon_2$  are the dielectric permittivities of metal and dielectric medium, respectively,  $v = c/\mu$  = speed of light in the dielectric medium,  $\mu$  -refractive index of dielectric medium.

To better understand the conditions for SPP excitation on fabricated samples, dispersion curves with  $k_{\text{inc}}$  and  $k_x$  on the corrugated samples Sa2 and Sa3 were plotted – Fig. 3a. Shorter corrugation period resulted in larger values of  $k_x$ . The dispersion curves of  $k_{\text{SPP}}$  based on eq.3 indicates that effective SPP coupling can occur at the Au/sapphire interface mediated by transmission diffraction orders [67–69]. Coupling between the diffracted orders  $k_x$  and the  $k_{\text{SPP}}$  at the Au/sapphire interface is marked by red dots in Fig. 3a. The first-order coupling of a SPP mode at 1.17 eV corresponds to the results of reflectance measurements of sample Sa2, showing a broad reflectance dip in the NIR region near 1040 nm (see Fig. 2b). We find similar trends for other corrugation periods in Figure S5 of the Supporting Information. The exponentially decaying electric field of the excited SPP extends to the Au/air interface to form coupled hybrid modes [70,71]. In our system (air/Au/Al<sub>2</sub>O<sub>3</sub> layer) the broadband reflectance dip in the IR region is related to an anti-symmetric SPP mode [72,73], Fig. 3b shows the simulated charge density polarization on the metal dielectric interfaces for TM polarization at  $\theta = 0^\circ$  and  $50^\circ$ . At  $\theta = 50^\circ$  the charge density polarization appears to be an a mixture of dipole moments that is typical of hybridized SPP mode at  $\lambda_{\text{exc}} = 785$  nm in Fig. 2c. The propagation of high-frequency symmetric mode is damped in the samples due to the discontinuous percolated network, which limits charge oscillations parallel to the surface [74]

and, by the Au intraband transitions in ultrathin films [32,74]. Furthermore, the nature of the broad reflectance dip is also attributed to the scattering on percolated grain boundaries. Considering this hybrid SPP excitation with low energy in the NIR region, these samples were investigated for SERS sensing of organic molecules. SERS measurements were performed for thiophenol as an analyte. The phenyl ring vibration modes assigned to the (C - C - C ring bend (ring breathing) and In-plane. C - C - C bend + C - S stretching) downshift upon the formation of phenyl thiolates (PT) [75], to 998  $\text{cm}^{-1}$  and 1072  $\text{cm}^{-1}$  confirming the chemisorption of thiophenol on the Au surface in sample Sa2 (Fig. 3c), where the blue arrow indicates the downshifting. Spectra collected from  $\lambda_{\text{exc}} = 785$  nm in Fig. 3c exhibited reduced interference background and prominent SERS as compared with  $\lambda_{\text{exc}} = 633$  nm. Such large intensity enhancement of PT peaks at  $\lambda_{\text{exc}} = 785$  nm are due to both the  $\lambda_{\text{exc}}$  and its related  $\lambda_{\text{stokes}}$  in (Table 2.), are closer to the  $\lambda_{\text{SPP}}$  resonance near 1040 nm in Fig. 3d. Moreover, chemisorbed aromatic thiols form S-Au bonds with the metal surface, causing charge transfer to occur at shorter excitation wavelengths hybridizing their molecular orbitals [6]. This causes intense fluorescence background and photo-reactions in thiolates [76]. Mapping the SERS intensity of sample Sa2 over a large area at  $\lambda_{\text{exc}} = 785$  nm confirmed that the intensity was uniform and photo-degradation of the molecule was minimal (Figure S7).

Further, Fig. 4a shows that the corrugated sample Sa2 exhibited a 46-fold SERS gain in the Raman active mode assigned to C - C - C ring bend (ring breathing (998  $\text{cm}^{-1}$ )) [85] versus the intensity of the mode collected from the flat Au sample Sa1. The SERS amplification of  $10^3$  orders measured on these samples in the experiment were analogous to the near-field enhancement of SPP modes described in Ref. [21,22] although SERS enhancement exhibited by the fabricated samples are lower as compared to NIR-SERS substrates exhibiting LSPR modes. The fabricated samples are suitable platforms to study molecule-polariton interaction through polarized SERS measurements, due to the large dipole oscillator strength of NIR-SPP fields and without the interference of charge transfer hybridizations and reduced photo-induced disadvantages at  $\lambda_{\text{exc}} = 785$  nm. The dependency of the SERS response of the adsorbed molecules on electric field polarization, and on different corrugation periods were investigated via polarized SERS measurements at  $\lambda_{\text{exc}} = 785$  nm.

Raman analysis performed between the incident polarization and  $k_{\text{corrugation}}$  (as in Fig. 4b) revealed an anisotropic SERS response for the sample Sa2. A 5-fold SERS intensity gain was observed at  $\sigma = 0^\circ$  for the peak at 998  $\text{cm}^{-1}$  versus the same peak at  $\sigma = 90^\circ$  (Fig. 4c). Moreover, at SERS intensity gain of the peak 998  $\text{cm}^{-1}$  at  $\sigma = 90^\circ$  was higher when compared to the flat sample. A similar anisotropic response was observed for samples Sa3 and Sa4, but the SERS gain of Raman modes decreased with increasing corrugation period - Fig. 4d. This effect was due to the larger difference between  $\lambda_{\text{exc}}$  and  $\lambda_{\text{SPP}}$ , and the increase in standard deviation  $\delta$  of the average corrugation period value  $P$ , resulting in a weaker SPP coupling.

In Fig. 5 polarized SERS measurements performed for  $\Delta\sigma = 2.5^\circ$  revealed a dichroic SERS anisotropy with  $\cos^2(\sigma)$  dependency for PT peaks assigned in Table 2. The relative Raman peaks intensities of anisotropic planar molecules such as the phenyl thiolates depend on the symmetry of the vibration modes [34]. The orientation of an adsorbed analyte's induced dipole moment can be different from incident light polarization, which influences analyte Raman modes relative SERS intensities [35]. The  $\cos^2(\sigma)$  based anisotropy was studied for phenyl thiolate Raman modes of different polarizability tensors on the corrugated plasmonic samples. For phenyl thiolates with a  $C_{2v}$  symmetry group, the  $a_1$  Raman modes are totally symmetric vibration with a combination of  $\alpha_{xx}$ ,  $\alpha_{yy}$  and  $\alpha_{zz}$  Raman tensors on the metal surface frame of reference, while the other  $b_1$ ,  $b_2$  and  $a_2$  non-totally symmetric vibration modes contain  $\alpha_{xz}$ ,  $\alpha_{yz}$  and  $\alpha_{xy}$  tensor components [38] - see Table 2. SERS anisotropy of the peak assigned to the symmetric in-plane C - C ring stretching at 1573  $\text{cm}^{-1}$  with  $a_1$  symmetry was more

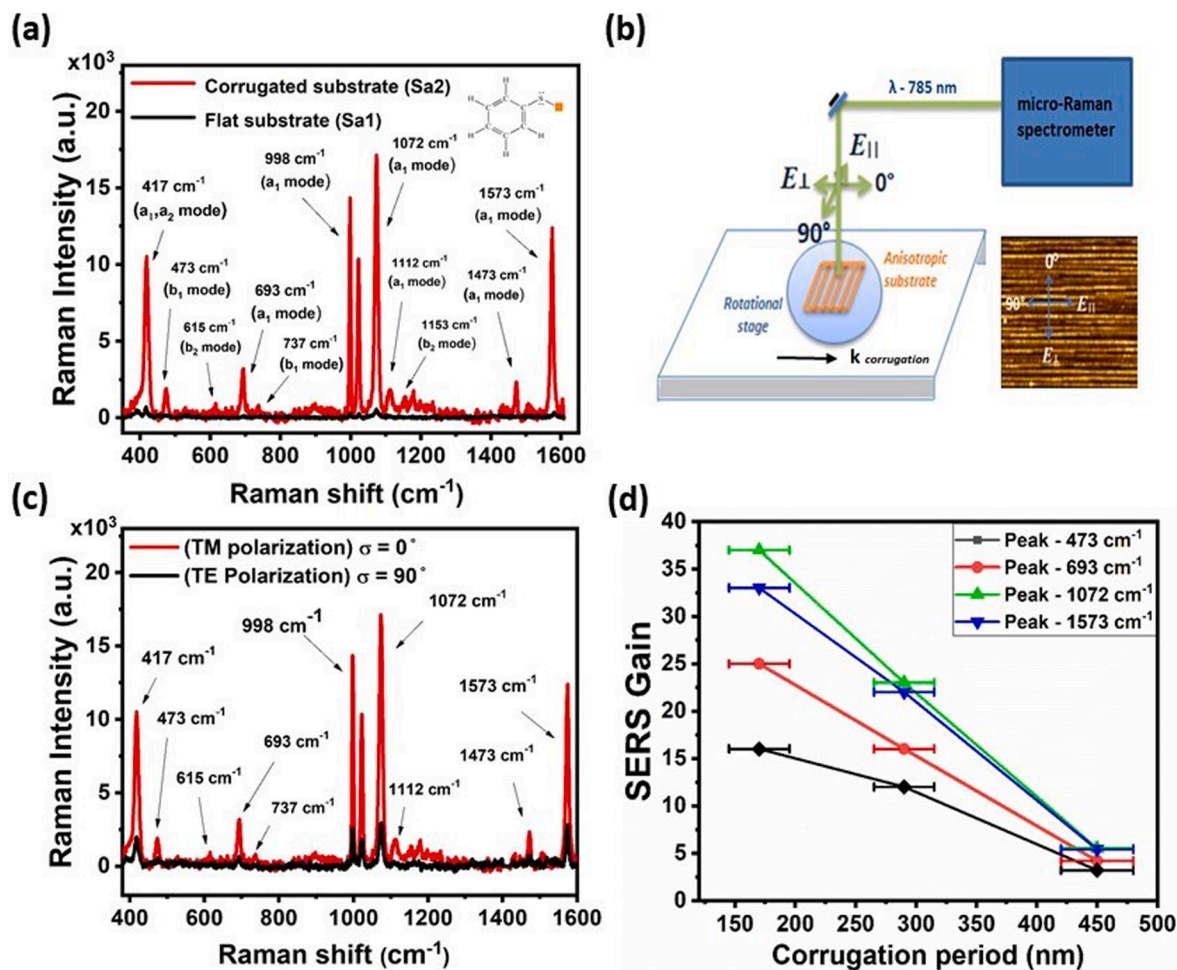


**Fig. 4.** (a) SERS spectra of phenyl thiolate on flat Sa1 (black line) and corrugated sample Sa2 (red line). Vibration modes assigned to Raman peaks with their symmetry classes are listed in Table 2, (b) Schematic drawing of the polarized SERS measurement setup with indicated angle  $\sigma$ . (c) Polarized SERS measurements performed for  $\sigma = 0^\circ$  and  $\sigma = 90^\circ$  laser polarizations on sample Sa2, (d) SERS Gain of selected phenylthiolate Raman vibrational peaks for different grating periodicity. (SERS gain calculations – supplementary information).

prominent and dependent on the corrugation period in Fig. 5a.

The anisotropy of peak assigned to the out-of-plane C–C–C bending at 473 cm<sup>-1</sup> with non-totally symmetric vibration b<sub>1</sub> mode exhibited less intensity compared to the a<sub>1</sub> mode and less pronounced dependence on the corrugation period in Fig. 5b. Electric field component E<sub>x</sub> parallel to the surface becomes large only during the SPP excitation along the k<sub>corrugation</sub> - Fig. 2c at  $\theta = 50^\circ$ , significantly exciting b<sub>1</sub> mode which has a  $\alpha_{xz}$  component with vibrational motion parallel to the surface along the k<sub>corrugation</sub>. Due to this a completely non-dichroic SERS behavior for peak 473 cm<sup>-1</sup> with b<sub>1</sub> mode was observed on sample Sa4 on which the  $\delta$  increases for both the height and width of the corrugated facets, resulting in weak SPP coupling and decrease in electric field strength along the x direction parallel to surface. Similar to b<sub>1</sub> mode less dependency on corrugation period was observed for the peak at 615 cm<sup>-1</sup> with b<sub>2</sub> mode in Fig. 5e but the peak was not observed for Sa1 and Sa4. Apart from the relative intensities of Raman active modes, the dichroic SERS behavior of Raman modes in Table 2. were determined mostly due to the excitation of SPP along the corrugation vector rather than the orientation of the analyte on the surface for a<sub>1</sub>, b<sub>1</sub> and b<sub>2</sub> modes – Fig. 5. The a<sub>2</sub> mode with  $\alpha_{xy}$  tensor component with both the axes in the plane of the surface was not observed on these anisotropic corrugated samples. Shorter corrugation periods fabricated exhibited pronounced SERS anisotropy in both totally symmetric (a<sub>1</sub>) and non-symmetric vibrations (b<sub>1</sub> and b<sub>2</sub>) modes versus the substrates with larger value of corrugation periods. This was due to the effective coupling of SPP mode at  $\sigma = 0^\circ$  for

Sa2. These experimental results shows the dependence of SPPs surface field orientation on corrugated plasmonic surface in enhancing both diagonal and non-diagonal component of molecules polarizability tensor. Moreover, SERS enhancement orders of the substrates can be further improved as metal thickness near percolation threshold supports both localized and delocalized surface plasmon resonance and can be used to manipulate optical absorption, scattering and light concentration near surfaces [63]. Optimizing plasmonic metal thickness below percolation threshold on these fabricated templates can further lead to uniaxial oriented plasmonic substrates such as self-assembled nanoparticle arrays for enhanced SERS performance.

#### 4. Conclusion

Corrugated thin-film plasmonic nanostructures supporting a hybrid SPP resonance in the NIR region was demonstrated. Thermally-induced large area surface reconstructed ( $\alpha$ -Al<sub>2</sub>O<sub>3</sub>) substrates with different periods were used as templates for percolated ultra-thin Au metal deposition. Reflectance analysis, electric field intensity ( $|E|^2$ ) distribution and charge density polarization simulations confirmed the coupling of an hybrid NIR-SPP mode for TM polarization at  $\theta = 50^\circ$ . A 46-fold SERS gain of phenyl thiolate (PT) peak 998 cm<sup>-1</sup> was observed on the corrugated samples when compared to a flat plasmonic sample. The observed spectra revealed a higher SERS at  $\lambda_{exc} = 785$  nm with reduced interference background, when compared to  $\lambda_{exc} = 633$  nm. The samples

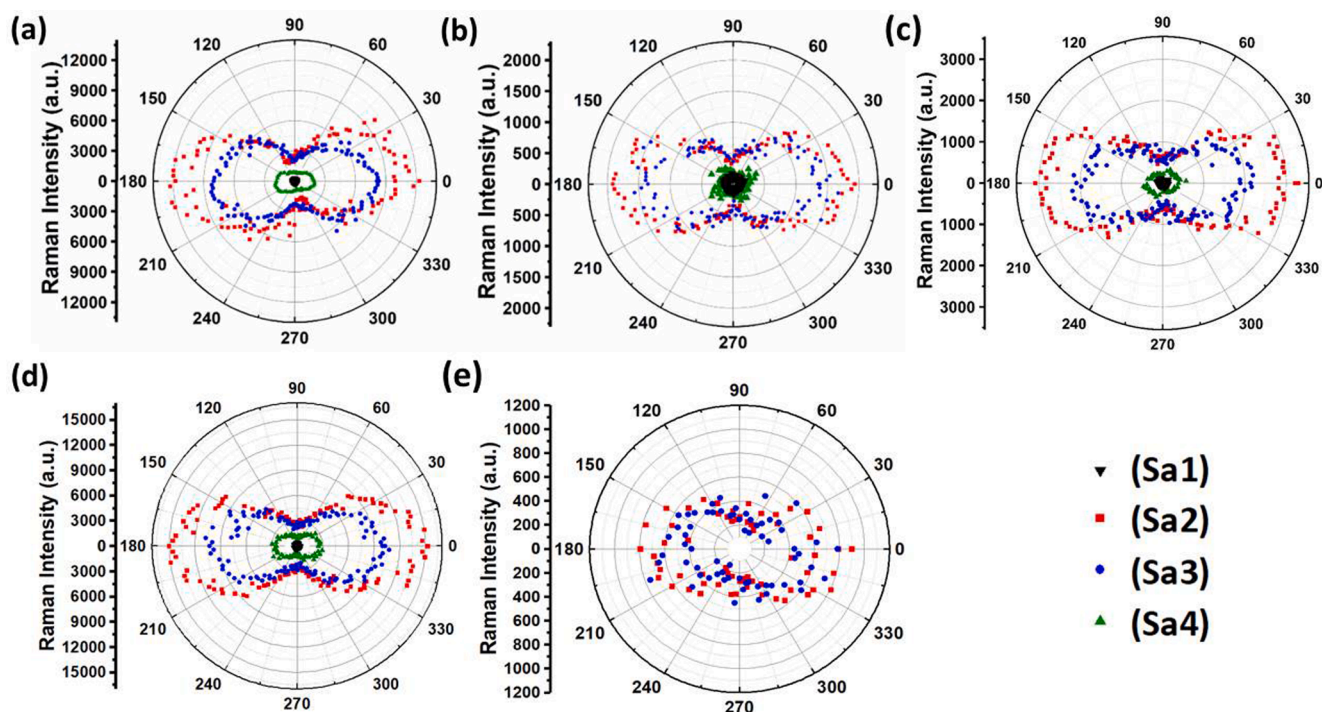


Fig. 5. Analysis of Raman intensity of selected thiophenol peaks in Table 2. (a)  $1573\text{ cm}^{-1}$ , (b)  $473\text{ cm}^{-1}$ , (c)  $693\text{ cm}^{-1}$ , (d)  $998\text{ cm}^{-1}$  and (e)  $615\text{ cm}^{-1}$  as a function of the azimuthal angle ( $\Delta\sigma = 2.5^\circ$ ) on flat and corrugated samples with different periods in polarized SERS measurements. (Table 2) depicts the symmetry modes corresponding to the Raman peaks analyzed ( $a_1$  are totally symmetric vibration), ( $b_1$ ,  $b_2$  and  $a_2$  non-totally symmetric vibrations).

were reproducible exhibiting large-area uniform sensing capability for the shorter corrugation periods due to effective coupling of SPP at  $\sigma = 0^\circ$  which spatially extends the SERS excitation volume. In polarized SERS analysis, a twofold SERS anisotropy with a  $\cos^2(\sigma)$  dependency ( $\sigma =$  azimuthal angle) was observed. A more pronounced dependence on corrugation period was observed for totally symmetric  $a_1$  modes than the non-totally symmetric  $b_1$  and  $b_2$  modes. Shorter corrugation periods fabricated exhibited pronounced SERS anisotropy of both totally symmetric ( $a_1$ ) and non-symmetric vibrations ( $b_1$  and  $b_2$ ) modes when comparing the substrates with larger value of corrugation periods this was due to the larger standard deviation  $\delta$  of period (P) for increasing corrugation periods resulting in a weaker SPP coupling. The SERS dichroism behaviour was determined mostly by the excitation of SPP along the  $k_{\text{corrugation}}$  rather than the orientation of the analyte on the laterally continuous corrugated surface for  $a_1$ ,  $b_1$  and  $b_2$  modes. We predict an edge-on orientation of the adsorbed molecule on the corrugated facets due to the absence of peak related to  $a_2$  mode with both vibration motions along the plane of the surface.

#### CRediT authorship contribution statement

**Ephraim T. Mathew:** Writing – original draft, Visualization, Validation, Software, Methodology, Investigation, Formal analysis, Data curation, Conceptualization, Writing – review & editing. **Jacek Jencyk:** Writing – review & editing, Methodology. **Zygmunt Miłosz:** Methodology. **Joel Henzie:** Writing – review & editing, Visualization, Software. **Igor Iatsunskyi:** Writing – review & editing, Investigation. **Patryk Florczak:** Methodology. **Weronika Andrzejewska:** Writing – review & editing, Visualization. **Mikołaj Lewandowski:** Writing – review & editing, Resources, Project administration, Methodology, Funding acquisition. **Maciej Wiesner:** Writing – original draft, Validation, Supervision, Resources, Methodology, Conceptualization, Writing – review & editing.

#### Declaration of competing interest

The authors declare that they have no known competing financial interests or personal relationships that could have appeared to influence the work reported in this paper.

#### Data availability

Data will be made available on request.

#### Acknowledgment

The studies were performed within the LaSensA project carried out under the M-ERA.NET 2 scheme (European Union Horizon 2020 research and innovation programme, grant No. 685451) and co-funded by the Research Council of Lithuania (LMTLT), agreement No. S-M-ERA.NET-21-2, the National Science Centre of Poland, project No. 2020/02/Y/ST5/00086, and the Saxon State Ministry for Science, Culture and Tourism (Germany), grant No. 100577922, as well as from the tax funds on the basis of the budget passed by the Saxon state parliament. E.M. acknowledges support from the IDUB Mini grant (internationalization of scientific research at the Doctoral School of the Adam Mickiewicz University, grant No. 054/13/SNŚ/0043). J.H. acknowledges support from the Japan Society for the Promotion of Science (JSPS) Grants-in-Aid for Scientific Research Kakenhi Program (20 K05453). I.I. acknowledges the financial support from NCN by the OPUS grant number 2020/37/B/ST5/00576 in the ellipsometry experiments of this article. The authors acknowledge and thank late Prof.dr hab. Stefan Jurga for leading the project during the initial phase.

#### Appendix A. Supplementary data

Supplementary data to this article can be found online at <https://doi.org/10.1016/j.apsusc.2024.159821>.



## References

- [1] J. Langer, D. Jimenez de Aberasturi, J. Aizpurua, R.A. Alvarez-Puebla, B. Auguie, J. J. Baumberg, G.C. Bazan, S.E.J. Bell, A. Boisen, A.G. Brolo, J. Choo, D. Cialla-May, V. Deckert, L. Fabris, K. Faulds, F.J. García de Abajo, R. Goodacre, D. Graham, A. J. Haes, C.L. Haynes, C. Huck, T. Itoh, M. Käll, J. Kneipp, N.A. Kotov, H. Kuang, E. C. Le Ru, H.K. Lee, J.F. Li, X.Y. Ling, S.A. Maier, T. Mayerhöfer, M. Moskovits, K. Murakoshi, J.M. Nam, S. Nie, Y. Ozaki, I. Pastoriza-Santos, J. Perez-Juste, J. Popp, A. Pucci, S. Reich, B. Ren, G.C. Schatz, T. Shegai, S. Schlücker, L.L. Tay, K. G. Thomas, Z.Q. Tian, R.P. Van Duyne, T. Vo-Dinh, Y. Wang, K.A. Willets, C. Xu, H. Xu, Y. Xu, Y.S. Yamamoto, B. Zhao, L.M. Liz-Marzán, Present and future of surface-enhanced raman scattering, *ACS Nano*. 14 (2020) 28–117, <https://doi.org/10.1021/acsnano.9b04224>.
- [2] A. Szaniawska, A. Kudelski, Applications of surface-enhanced raman scattering in biochemical and medical analysis, *Front Chem.* 9 (2021), <https://doi.org/10.3389/fchem.2021.664134>.
- [3] S.Y. Ding, E.M. You, Z.Q. Tian, M. Moskovits, Electromagnetic theories of surface-enhanced raman spectroscopy, *Chem Soc Rev.* 46 (2017) 4042–4076, <https://doi.org/10.1039/c7cs00238f>.
- [4] K.S. Menghrajani, M. Chen, K. Dholakia, W.L. Barnes, Probing vibrational strong coupling of molecules with wavelength-modulated raman spectroscopy, *Adv Opt Mater.* 10 (2022), <https://doi.org/10.1002/adom.202102065>.
- [5] M.L. McGlashen, U. Guhathakurta, K.L. Davis, M.D. Morris, S.E.R.S. Microscopy, Laser illumination effects, *Appl. Spectrosc.* 45 (1991) 543–545, <https://doi.org/10.1366/000370291436976>.
- [6] R.A. Álvarez-Puebla, Effects of the excitation wavelength on the SERS spectrum, *J. Phys. Chem. Lett.* 3 (2012) 857–866, <https://doi.org/10.1021/jz201625j>.
- [7] D. Cebeci-Maltaş, P. Wang, M.A. Alam, R. Pinal, D. Ben-Amotz, Photobleaching profile of raman peaks and fluorescence background, *Eur. Pharm. Rev.* 22 (2017) 18–21.
- [8] M. Škrabić, M. Kosović, M. Gotić, L. Mikac, M. Ivanda, O. Gamulin, Near-infrared surface-enhanced raman scattering on silver-coated porous silicon photonic crystals, *Nanomaterials*. 9 (2019), <https://doi.org/10.3390/nano9030421>.
- [9] A. Kudelski, J. Bukowska, Influence of photochemical effects on irreversible loss of “active sites” on SERS active silver electrode, *Spectrochim Acta A*. 51 (1995) 573–578, [https://doi.org/10.1016/0584-8539\(94\)00170-G](https://doi.org/10.1016/0584-8539(94)00170-G).
- [10] M.D. Doherty, A. Murphy, J. McPhillips, R.J. Pollard, P. Dawson, Wavelength dependence of raman enhancement from gold nanorod arrays: quantitative experiment and modeling of a hot spot dominated system, *J. Phys. Chem. C* 114 (2010) 19913–19919, <https://doi.org/10.1021/jp107063x>.
- [11] R.V. Nair, V.M. Murukeshan, (Cu<sub>2</sub>O–Au) – graphene – Au layered structures as efficient near infra - red SERS substrates, *Sci Rep.* 10 (2020), <https://doi.org/10.1038/s41598-020-60874-x>.
- [12] S.M. Angel, L.F. Katz, D.D. Archibald, L.T. Lin, D.E. Honigs, Near-infrared surface-enhanced raman spectroscopy. part I: copper and gold electrodes, *Appl. Spectrosc.* 42 (1988) 1327–1331, <https://doi.org/10.1366/0003702884429698>.
- [13] K. Kneipp, Y. Wang, R.R. Dasari, M.S. Feld, Near-infrared surface-enhanced raman scattering (NIR-SERS) of neurotransmitters in colloidal silver solutions, *Spectrochim Acta A Mol Biomol Spectrosc.* 51 (1995) 481–487, [https://doi.org/10.1016/0584-8539\(94\)00235-4](https://doi.org/10.1016/0584-8539(94)00235-4).
- [14] K. Kneipp, E. Roth, C. Engert, W. Kiefer, Near-infrared excited surface-enhanced raman spectroscopy of rhodamine 6G on colloidal silver, *Chem Phys Lett.* 207 (1993) 450–454, [https://doi.org/10.1016/0009-2614\(93\)89028-G](https://doi.org/10.1016/0009-2614(93)89028-G).
- [15] F. Muniz-Miranda, A. Pedone, M. Muniz-Miranda, Raman and computational study on the adsorption of xanthine on silver nanocolloids, *ACS Omega*. 3 (2018) 13530–13537, <https://doi.org/10.1021/acsomega.8b02174>.
- [16] C. Deriu, S. Thakur, O. Tammaro, L. Fabris, Challenges and opportunities for SERS in the infrared: materials and methods, *Nanoscale Adv.* 5 (2023) 2132–2166, <https://doi.org/10.1039/d2na00930g>.
- [17] D. Mortazavi, A.Z. Kouzani, A. Kaynak, W. Duan, DEVELOPING LSPR DESIGN GUIDELINES, 2012.
- [18] N.R. Agarwal, F. Neri, S. Trusso, A. Lucotti, P.M. Ossi, Au nanoparticle arrays produced by pulsed laser deposition for surface enhanced Raman spectroscopy, *Appl Surf Sci* 258 (23) (2012) 9148–9152, <https://doi.org/10.1016/j.apsusc.2011.12.030>.
- [19] B. Moll, T. Tichelkamp, S. Wegner, B. Francis, T.J.J. Müller, C. Janiak, Near-infrared (NIR) surface-enhanced raman spectroscopy (SERS) study of novel functional phenothiazines for potential use in dye sensitized solar cells (DSSC), *RSC Adv.* 9 (2019) 37365–37375, <https://doi.org/10.1039/c9ra08675g>.
- [20] N. Micali, F. Neri, P.M. Ossi, S. Trusso, Light scattering enhancement in nanostructured silver film composites, *J. Phys. Chem. C*. 117 (2013) 3497–3502, <https://doi.org/10.1021/jp3125507>.
- [21] J. Homola, Electromagnetic theory of surface plasmons, *Surface plasmon resonance based sensors* (2006) 3–44, [https://doi.org/10.1007/5346\\_013](https://doi.org/10.1007/5346_013).
- [22] W.H. Weber, G.W. Ford, Optical electric-field enhancement at a metal surface arising from surface-plasmon excitation, 1981.
- [23] N. Coca-López, N.F. Hartmann, T. Mancabelli, J. Kraus, S. Günther, A. Comin, A. Hartschuh, Remote excitation and detection of surface-enhanced raman scattering from graphene, *Nanoscale*. 10 (2018) 10498–10504, <https://doi.org/10.1039/c8nr02174k>.
- [24] P. Xu, S.H. Jeon, N.H. MacK, S.K. Doorn, D.J. Williams, X. Han, H.L. Wang, Field-assisted synthesis of SERS-active silver nanoparticles using conducting polymers, *Nanoscale*. 2 (2010) 1436–1440, <https://doi.org/10.1039/c0nr00106f>.
- [25] P. Xu, B. Zhang, N.H. MacK, S.K. Doorn, X. Han, H.L. Wang, Synthesis of homogeneous silver nanosheet assemblies for surface enhanced raman scattering applications, *J Mater Chem.* 20 (2010) 7222–7226, <https://doi.org/10.1039/c0jm01322f>.
- [26] M.O. Sallam, G.A.E. Vandenbosch, G. Gielen, E.A. Soliman, Integral equations formulation of plasmonic transmission lines, *Opt Express*. 22 (2014) 22388, <https://doi.org/10.1364/oe.22.022388>.
- [27] Y. Fang, M. Sun, Nanoplasmonic waveguides: towards applications in integrated nanophotonic circuits, *Light Sci Appl.* 4 (2015), <https://doi.org/10.1038/lsa.2015.67>.
- [28] R.S. Anwar, H. Ning, L. Mao, Recent advancements in surface plasmon polaritons-plasmonics in subwavelength structures in microwave and terahertz regimes, *Digital Communications and Networks* 4 (2018) 244–257, <https://doi.org/10.1016/j.dcan.2017.08.004>.
- [29] R. Sakuma, K.T. Lin, S. Kim, F. Kimura, Y. Kajihara, Passive near-field imaging via grating-based spectroscopy, *Rev. Sci. Instrum.* 93 (2022), <https://doi.org/10.1063/1.50059498>.
- [30] R. Gabai, A. Ismach, E. Joselevich, Nanofacet lithography: a new bottom-up approach to nanopatterning and nanofabrication by soft replication of spontaneously faceted crystal surfaces, *Adv. Mater.* 19 (2007) 1325–1330, <https://doi.org/10.1002/adma.200601625>.
- [31] J.R. Heffelfinger, M.W. Bench, C.B. Carter, On the faceting of ceramic surfaces, *Surf Sci.* 343 (1995), [https://doi.org/10.1016/0039-6028\(95\)00896-9](https://doi.org/10.1016/0039-6028(95)00896-9).
- [32] M. Barelli, M.C. Giordano, P.G. Gucciardi, F. Buatier De Mongeot, Self-organized nanogratings for large-area surface plasmon polariton excitation and surface-enhanced raman spectroscopy sensing, *ACS Appl Nano Mater.* 3 (2020) 8784–8793, <https://doi.org/10.1021/acsnm.0c01569>.
- [33] Y. Liu, H. Zhang, Y. Geng, S. Xu, W. Xu, J. Yu, W. Deng, B. Yu, L. Wang, Long-range surface plasmon resonance configuration for enhancing SERS with an adjustable refractive index sample buffer to maintain the symmetry condition, *ACS Omega*. 5 (2020) 32951–32958, <https://doi.org/10.1021/acsomega.0c03923>.
- [34] J.A. Creighton, Surface raman electromagnetic enhancement factors for molecules at the surface of small isolated metal spheres: the determination of adsorbate orientation from Sers relative intensities, *Surf Sci.* 124 (1983) 209–219, [https://doi.org/10.1016/0039-6028\(83\)90345-X](https://doi.org/10.1016/0039-6028(83)90345-X).
- [35] M. Moskovits, J.S. Suh, Surface selection rules for surface-enhanced raman spectroscopy: calculations and application to the surface-enhanced raman spectrum of phthalazine on silver, *J Phys Chem.* 88 (1984) 5526–5530, <https://doi.org/10.1021/j150667a013>.
- [36] M. Moskovits, Surface selection rules, *J Chem Phys.* 77 (1982) 4408–4416, <https://doi.org/10.1063/1.444442>.
- [37] D.J. Walls, P.W. Bohn, Enhanced raman scattering at dielectric surfaces. 2, Molecular Orientations from Polarized Surface Raman Scattering, *J. Phys. Chem.* 94 (5) (1990) 2039–2042, <https://doi.org/10.1021/j100368a058>.
- [38] K.T. Carron, L.G. Hurley, Axial and azimuthal angle determination with surface-enhanced Raman spectroscopy: thiophenol on copper, silver, and gold metal surfaces, *J. Phys. Chem.* 95 (24) (1991) 9979–9984, <https://doi.org/10.1021/j100177a068>.
- [39] L.J. Wan, M. Terashima, H. Noda, M. Osawa, Molecular orientation and ordered structure of benzenethiol adsorbed on gold(111), *J. Phys. Chem. B*. 104 (2000) 3563–3569, <https://doi.org/10.1021/jp993328r>.
- [40] B. Fazio, C. D'Andrea, F. Bonaccorso, A. Irrera, G. Calogero, C. Vasi, P.G. Gucciardi, M. Allegrini, A. Toma, D. Chiappe, C. Martella, F., Buatier de mongeot, re-radiation enhancement in polarized surface-enhanced resonant raman scattering of randomly oriented molecules on self-organized gold nanowires, *ACS Nano*. (2011) 5945–5956, <https://doi.org/10.1021/nn201730k>.
- [41] R. Arul, K. Menghrajani, M.S. Rider, R. Chikkaraddy, W.L. Barnes, J.J. Baumberg, Raman probing the local ultrastrong coupling of vibrational plasmon polaritons on metallic gratings, *Phys. Rev. Lett* 131 (12) (2023) 126902.
- [42] C.Y. Chan, Z.L. Cao, H.C. Ong, Study of coupling efficiency of molecules to surface plasmon polaritons in surface-enhanced raman scattering (SERS), *Opt Express*. 21 (2013) 14674, <https://doi.org/10.1364/oe.21.014674>.
- [43] M.S. Rider, R. Arul, J.J. Baumberg, W.L. Barnes, Theory of strong coupling between molecules and surface plasmons on a grating, *Nanophotonics*. 11 (2022) 3695–3708, <https://doi.org/10.1515/nanoph-2022-0301>.
- [44] W.L. Barnes, S. Wedge, Surface plasmon polariton mediated emission of light, in: *Photonic Crystal Materials and Nanostructures*, Vol. 5450, SPIE, 2004, pp. 412–415, <https://doi.org/10.1117/12.555934>.
- [45] G. Winter, S. Wedge, W.L. Barnes, Can lasing at visible wavelengths be achieved using the low-loss long-range surface plasmon-polariton mode? *New J Phys.* 8 (2006) <https://doi.org/10.1088/1367-2630/8/8/125>.
- [46] C. Zanchi, A. Lucotti, M. Tommasini, M. Pistaffa, L. Giuliani, S. Trusso, P.M. Ossi, Pulsed laser deposition of gold thin films with long-range spatial uniform SERS activity, *Appl Phys A Mater Sci Process.* 125 (2019), <https://doi.org/10.1007/s00339-019-2527-7>.
- [47] C. D'Andrea, A. Irrera, B. Fazio, A. Foti, E. Messina, O.M. Maragò, S. Kessentini, P. Artoni, C. David, P.G. Gucciardi, Red shifted spectral dependence of the SERS enhancement in a random array of gold nanoparticles covered with a silica shell: extinction versus scattering, *Journal of Optics (United Kingdom)*. 17 (2015), <https://doi.org/10.1088/2040-8978/17/11/114016>.
- [48] D. Repetto, M.C. Giordano, A. Foti, P.G. Gucciardi, C. Mennucci, F. Buatier de Mongeot, SERS amplification by ultra-dense plasmonic arrays on self-organized PDMS templates, *Appl Surf Sci.* 446 (2018) 83–91, <https://doi.org/10.1016/j.apsusc.2018.02.163>.
- [49] C. D'Andrea, J. Bochterle, A. Toma, C. Huck, F. Neubrech, E. Messina, B. Fazio, O. M. Maragò, E. Di Fabrizio, M. Lamy De La Chapelle, P.G. Gucciardi, A. Pucci, Optical nanoantennas for multiband surface-enhanced infrared and raman



- spectroscopy, *ACS Nano*. 7 (2013) 3522–3531, <https://doi.org/10.1021/nm4004764>.
- [50] G. Rosenblatt, B. Simkhovich, G. Bartal, M. Orenstein, Nonmodal plasmonics: controlling the forced optical response of nanostructures, *Phys Rev X*. 10 (2020), <https://doi.org/10.1103/PhysRevX.10.011071>.
- [51] E.D. Palik, Aluminum oxide revisited, in: *Handbook of Optical Constants of Solids*, 1998.
- [52] D. Issaad, H. Moustau, A. Medjahed, L. Lalaoui, J. Spadavecchia, M. Bouafia, M. L. De La Chapelle, N. Djaker, Scattering correlation spectroscopy and raman spectroscopy of thiophenol on gold nanoparticles: comparative study between nanospheres and nanourchins, *J. Phys. Chem. C* 121 (2017) 18254–18262, <https://doi.org/10.1021/acs.jpcc.7b05355>.
- [53] D.J. Erb, J. Perlich, S.V. Roth, R. Röhlberger, K. Schlage, Real-time observation of temperature-induced surface nanofaceting in M-plane  $\alpha$ -Al<sub>2</sub>O<sub>3</sub>, *ACS Appl Mater Interfaces*. 14 (2022) 31373–31384, <https://doi.org/10.1021/acami.1c20209>. J. R.
- [54] X. Ou, Y. Liu, M. Zhang, L. Hua, S. Zhan, Plasmonic Gold Nanostructures for Biosensing and Bioimaging, *Mikrochim. Acta*. 188 (2019) 304, <https://doi.org/10.1007/s00604-021-04964-1/Published>.
- [55] P.K. Jain, K.S. Lee, I.H. El-Sayed, M.A. El-Sayed, Calculated absorption and scattering properties of gold nanoparticles of different size, shape, and composition: applications in biological imaging and biomedicine, *J. Phys. Chem. B* 110 (2006) 7238–7248, <https://doi.org/10.1021/jp057170o>.
- [56] D. Eschimese, P. Hsia, F. Vaurette, D. Deresmes, P. De Bettignies, J. Schreiber, M. Chaigneau, S. Arscott, G. Lèveque, T. Mélin, Comparative investigation of plasmonic properties between tunable nanoobjects and metallized nanopores for optical spectroscopy, *J. Phys. Chem. C* (2019), <https://doi.org/10.1021/acs.jpcc.9b09977>.
- [57] R.A. Maniyara, D. Rodrigo, R. Yu, J. Canet-Ferrer, D.S. Ghosh, R. Yongsunthorn, D. E. Baker, A. Rezikyan, F.J. García de Abajo, V. Pruneri, Tunable plasmons in ultrathin metal films, *Nat Photonics*. 13 (2019) 328–333, <https://doi.org/10.1038/s41566-019-0366-x>.
- [58] K. Seal, M.A. Nelson, Z.C. Ying, D.A. Genov, A.K. Sarychev, V.M. Shalae, Growth, morphology, and optical and electrical properties of semicontinuous metallic films, *Phys Rev B Condens Matter Mater Phys*. 67 (2003), <https://doi.org/10.1103/PhysRevB.67.035318>.
- [59] D.A. Genov, V.M. Shalae, A.K. Sarychev, Surface plasmon excitation and correlation-induced localization–delocalization transition in semicontinuous metal films, *Phys Rev B Condens Matter Mater Phys*. 72 (2005), <https://doi.org/10.1103/PhysRevB.72.113102>.
- [60] M. Liszewska, B. Budner, M. Norek, B.J. Jankiewicz, P. Nyga, Revisiting semicontinuous silver films as surface-enhanced raman spectroscopy substrates, *Beilstein, J. Nanotechnology*. 10 (2019) 1048–1055, <https://doi.org/10.3762/BJNANO.10.105>.
- [61] E. Hedl, V.B. Bregović, I.Š. Rakić, Š. Mandić, Ž. Samec, A. Bergmann, J. Sancho-Parramon, Optical properties of annealed nearly percolated Au thin films, *Opt Mater (amst)*. 135 (2023), <https://doi.org/10.1016/j.optmat.2022.113237>.
- [62] A.B. Tesler, B.M. Maoz, Y. Feldman, A. Vaskevich, I. Rubinstein, Solid-state thermal dewetting of just-percolated gold films evaporated on glass: development of the morphology and optical properties, *J. Phys. Chem. C* 117 (2013) 11337–11346, <https://doi.org/10.1021/jp400895z>.
- [63] Y.L. Wang, F. Nan, X.L. Liu, L. Zhou, X.N. Peng, Z.K. Zhou, Y. Yu, Z.H. Hao, Y. Wu, W. Zhang, Q.Q. Wang, Z. Zhang, Plasmon-enhanced light harvesting of chlorophylls on near-percolating silver films via one-photon anti-stokes upconversion, *Sci Rep*. 3 (2013), <https://doi.org/10.1038/srep01861>.
- [64] G.R. Parkins, W.E. Lawrence, R.W. Christy, Intraband optical conductivity  $\sigma(\omega, T)$  of Cu, Ag, and Au: contribution from electron-electron scattering, *Phys Rev B*. 23 (1981) 6408, <https://doi.org/10.1103/PhysRevB.23.6408>.
- [65] Y. Kalachyova, D. Mares, O. Lyutakov, M. Kostejn, L. Lapeck, V. Švorčík, Surface plasmon polaritons on silver gratings for optimal SERS response, *J. Phys. Chem. C* 119 (2015) 9506–9512, <https://doi.org/10.1021/acs.jpcc.5b01793>.
- [66] H. Raether, G. Hohler, E.A. Niekisch, Surface plasmons on smooth and rough surfaces and on gratings, 111, Springer Tracts in Modern Physics, 1988, <https://doi.org/10.1007/BFb0048317>.
- [67] B.K. Singh, A.C. Hillier, Surface plasmon resonance enhanced transmission of light through gold-coated diffraction gratings, *Anal Chem*. 80 (2008) 3803–3810, <https://doi.org/10.1021/ac800045a>.
- [68] A. Baba, K. Kanda, T. Ohno, Y. Ohdaira, K. Shinbo, K. Kato, F. Kaneko, Multimode surface plasmon excitations on organic thin film/metallic diffraction grating, *Jpn J Appl Phys*. 49 (2010), <https://doi.org/10.1143/JJAP.49.01AE02>.
- [69] R. Mahmood, M.B. Johnson, A.C. Hillier, Massive enhancement of optical transmission across a thin metal film via wave vector matching in grating-coupled surface plasmon resonance, *Anal Chem*. 91 (2019) 8350–8357, <https://doi.org/10.1021/acs.analchem.9b01148>.
- [70] Z. Chen, K. Feng, Z. Chen, J. Shen, H. Li, Surface-enhanced raman scattering on silver sinusoidal nanograting: impact of interactions of grating-coupled surface plasmon polaritons, *Plasmonics*. 17 (2022) 757–764, <https://doi.org/10.1007/s11468-021-01587-3>.
- [71] J.J. Burke, G.I. Stegeman, T. Tamir, Surface-polariton-like waves guided by thin, lossy metal films, *Phys Rev B*. 33 (1986) 5186–5201, <https://doi.org/10.1103/PhysRevB.33.5186>.
- [72] Z. Lenac, M.S. Tomaš, Attenuation of long-range surface polaritons in a thin metallic slab with a dielectric coating, *Surf Sci*. 154 (1985) 639–657, [https://doi.org/10.1016/0039-6028\(85\)90055-X](https://doi.org/10.1016/0039-6028(85)90055-X).
- [73] M. Fukui, V.C.Y. So, R. Normandin, Lifetimes of surface plasmons in thin silver films, *Phys. Status Solidi B*. 91 (1979) K61–K64, <https://doi.org/10.1002/pssb.2220910159>.
- [74] A. Salwén, L. Stensland, Spectral filtering possibilities of surface plasma oscillations in thin metal films, *Opt Commun*. 2 (1970) 9–13, [https://doi.org/10.1016/0030-4018\(70\)90018-0](https://doi.org/10.1016/0030-4018(70)90018-0).
- [75] S.K. Saikin, Y. Chu, D. Rappoport, K.B. Crozier, A. Aspuru-Guzik, Separation of electromagnetic and chemical contributions to surface-enhanced raman spectra on nanoengineered plasmonic substrates, *J. Phys. Chem. Lett*. 1 (2010) 2740–2746, <https://doi.org/10.1021/jz1008714>.
- [76] J. Ye, J.A. Hutchison, H. Uji-i, J. Hofkens, L. Lagae, G. Maes, G. Borghs, P. Van Dorpe, Excitation wavelength dependent surface enhanced raman scattering of 4-aminothiophenol on gold nanorings, *Nanoscale*. 4 (2012) 1606, <https://doi.org/10.1039/c2nr11805j>.
- [77] F. Madzharova, Z. Heiner, J. Kneipp, Surface-enhanced hyper raman spectra of aromatic thiols on gold and silver nanoparticles, *J. Phys. Chem. C* 124 (2020) 6233–6241, <https://doi.org/10.1021/acs.jpcc.0c00294>.